Asian Journal of Chemistry; Vol. 37, No. 6 (2025), 1392-1398

ASIAN JOURNAL OF CHEMISTRY

https://doi.org/10.14233/ajchem.2025.33777

Photocatalytic Performance of SnO_2 Nanoparticles for the Efficient Degradation of Chlorpyrifos Pesticide Under Visible Light Irradiation

PANDURANGAN VIJAYALAKSHMI[1], RAMANA GANGIREDDY[2], LAKSHMI THANGAVELU[3,*] and S. VISNU[4]

[1]Department of Radiology, Saveetha Medical College and Hospital, Saveetha Institute of Medical and Technical Sciences, Thandalam, Chennai-602105, India
[2]Department of Pharmaceutics and Biotechnology, K.V.S.R. Siddhartha College of Pharmaceutical Sciences, Vijayawada-520008, India
[3]Center for Global Health Research, Saveetha Medical College, Saveetha Institute of Medical and Technical Sciences, Saveetha University, Chennai-602105, India
[4]Department of Orthopaedics, Saveetha Medical College and Hospital, Saveetha Institute of Medical and Technical Sciences, Thandalam, Chennai-602105, India

*Corresponding author: E-mail: lakshmi@saveetha.com

Received: 20 March 2025; *Accepted*: 5 May 2025; *Published online*: 27 May 2025; AJC-22013

Heterostructured semiconductor photocatalysts have demonstrated exceptional adsorption capabilities for organic pollutants, making them highly effective for environmental purification. In this study, SnO_2 nanoparticles were synthesized using the hydrothermal method and examined as a potential photocatalyst. The synthesized nanoparticles were analyzed using X-ray diffraction (XRD), Fourier transform infrared spectroscopy (FTIR), scanning electron microscopy (SEM), UV-visible spectroscopy and photoluminescence (PL) spectroscopy. The degradation of chlorpyrifos was monitored to evaluate the photocatalytic efficiency of SnO_2 revealing that 78.8% of chlorpyrifos was eliminated within 90 min using 50 mg of photocatalyst with an initial pollutant concentration of 20 ppm. Scavenger tests were conducted to identify the reactive species involved in the photocatalytic process. Furthermore, the recyclability of the photocatalyst was assessed with a fresh chlorpyrifos sample, showing a decrease in degradation efficiency from 78.8% to 67.7%, confirming the efficient reusability of SnO_2 nanoparticles and their high photocatalytic performance under visible light irradiation.

Keywords: Photocatalysis, SnO_2 nanoparticle, Chlorpyrifos degradation, Visible light irradiation, Hydrothermal synthesis.

INTRODUCTION

Water pollution is a major global issue that worsens annually, causing severe and often irreversible damage to the environment. The scarcity of potable water threatens all living organisms, including over 1.2 billion people worldwide [1,2]. Consequently, developing technologies to purify wastewater and produce clean water is crucial [3,4]. Water contamination primarily results from excessive pesticide use, pharmaceutical residues, oils and industrial waste [5]. Among industrial discharges, organic pollutants such as solvents, pesticides and dyes are the most concerning due to their toxic and hazardous nature, drawing significant attention from researchers [6,7]. Currently, over a thousand types of pesticides are produced in massive quantities each year [8]. These are extensively utilized in industries like paint, cosmetics and textiles, where their waste severely deteriorates ecosystems. Pesticides are linked to the allergic reactions, dermatitis, skin irritation, cancer and even genetic mutations in humans [9].

Metal oxide nanoparticles have found widespread applications in various fields, including medicine, electronics, catalysis, cosmetics, storage devices, biomedicine and drug delivery systems [10]. In particular, transition metal-based metal oxide nanoparticles have garnered immense interest among scientists due to their unique physical and chemical characteristics, attributed to their edge surface sites and nanoscale dimensions [11,12]. Several transition metal oxides have been synthesized by researchers, including zinc oxide (ZnO) [13], titanium dioxide (TiO_2) [14], selenium oxide (SeO_2) [15], copper iron oxide ($CuFe_2O_4$) [16], nickel oxide (NiO) [17], cobalt oxide (Co_3O_4) [18], *etc*. Among these, SnO_2 has attracted considerable attention due to its n-type semiconductor behaviour, featuring a band gap of 3.6 eV at room temperature. It exhibits exceptional optical and electrical properties, such as high optical transparency and low resistivity. The electron mobility in SnO_2 is notably high, ranging between 100 and 200 $cm^2 V^{-1} s^{-1}$, facilitating rapid transport of photoexcited electrons compared to other transition metal oxides [8,19].

Due to these remarkable properties, SnO_2 has been extensively employed in the development of rechargeable lithium batteries, gas sensors, electrocatalysts and photocatalysts [4]. The synthesis of SnO_2 nanoparticles has been a topic of great interest among researchers, leading to the adoption of various fabrication techniques. Utilized the co-precipitation method to produce SnO_2 nanoparticles with an average diameter of 3.2 nm, the synthesized SnO_2 nanocrystals with sizes ranging from 2.8 to 5.1 nm using the sol-gel process [20]. Similarly, Chen & Gao [21] employed the hydrothermal method to obtain SnO_2 nanoparticles with a 3.0 nm diameter, synthesized SnO_2 nanocrystals with diameters between 4 and 5 nm *via* the microwave combustion technique. Several existing studies have reported SnO_2 nanoparticles with broad size distributions and less controlled morphologies [22]. To address these challenges, several researchers have employed capping ligands to stabilize SnO_2 nanoparticles [23].

The present study bridges this gap by reporting the synthesis of SnO_2 nanoparticles with a narrow size distribution, eliminating the requirement for capping ligands [24]. This work holds significant importance in terms of controlled morphological synthesis and practical applications of SnO_2 nanoparticles [9]. It utilized SnO_2 nanowires as catalysts in lithium-ion batteries, while employed SnO_2 nanopowder in gas sensors, incorporated SnO_2 mesoporous spheres as photoanode materials in solar cells. Furthermore, the small particle size of SnO_2 nanoparticles significantly enhances their surface area, thereby improving photocatalytic efficiency by facilitating electron–hole separation [25].

In this study, SnO_2 nanoparticles were synthesized *via* a simple hydrothermal method using $SnCl_2$ as a precursor. The synthesized product was characterized through X-ray diffraction (XRD) and scanning electron microscopy (SEM). Furthermore, a formation mechanism explaining the transition from a tetragonal unit cell to cube-like morphology is discussed. The study also investigates the application of synthesized SnO_2 nanoparticles demonstrated the photocatalytic potential of SnO_2 nanoparticles in the degradation of chlorpyrifos, which is an organophosphate pesticide known for its neurotoxic effects, as it inhibits the acetylcholinesterase enzyme, leading to severe disruptions in the nervous system and hormonal imbalances in living organisms.

EXPERIMENTAL

All the chemicals and reagents utilized in this study were of analytical grade (A.R.) and used without any additional purification. Hydrated stannic chloride ($SnCl_4·5H_2O$) and sodium hydroxide (NaOH) were procured from Sigma-Aldrich, USA. Deionized water was employed throughout the experimental procedures. Isopropyl alcohol (IPA, Sigma-Aldrich), 1,4-benzoquinone (BQ, Alfa Aesar, USA) and potassium iodide (KI) were acquired from Sigma-Aldrich and used for the scavenger test. The pesticide Chlorpyrifos (CPF-500 mL) was sourced from IndiaMART and utilized as a pollutant. Both Millipore distilled water and deionized water were used during the experiment.

Synthesis of SnO_2 nanoparticles: SnO_2 nano-spherical-like architectures were synthesized using a straightforward hydrothermal method. A 1 M of hydrated stannic chloride (50 mL) was prepared and its pH was adjusted to 10 by adding a 2 M NaOH, resulting in the formation of a milky suspension. This mixture was stirred for 30 min at room temperature before being transferred into a Teflon-lined stainless steel hydrothermal reactor and maintained at 150 ºC for 24 h. The resulting precipitates were collected *via* centrifugation and thoroughly washed with distilled water and methanol to eliminate any impurities. The obtained precipitates were then dried in an oven at 80 ºC overnight. Finally, the dried product was ground into a fine powder and calcined at 600 ºC for 3 h in an electric furnace [12,26].

Characterization: The synthesized nanoparticle was analyzed using an X-ray Diffractometer (Bruker Kappa APEX II) to determine their crystalline phase structure and phase composition, employing Cu*K*α radiation over a 2θ range of 10-80º. The surface morphology, elemental mapping distribution, internal structure (including particle size, shape and dispersion), surface chemical bonding and optical characteristics of the nanocomposite were investigated through high-resolution scanning electron microscopy (HRSEM, FEI-Quanta FEG 200F) and UV-vis diffuse reflectance spectroscopy (DRS, Shimadzu/UV 2600 UV-vis spectrophotometer, ranging from 400 to 800 nm). Photoluminescence (PL) spectra were recorded using an Edinburgh FL/FS900 spectrophotometer with an excitation wavelength of 320 nm to analyze the interaction between the elements within the nanocomposite.

Photocatalytic degradation of organic pollutants: The photocatalytic breakdown of organic contaminants such as CPF was conducted in a photocatalytic reactor (Heber photoreactor, Annular type, HVAR-MP400) under UV-visible light exposure using a 300 W Xenon lamp and a 420 nm cut-off filter, which entirely blocks radiation below 420 nm [20]. Initially, 50 mg of synthesized SnO_2 nanocomposite was introduced into 100 mL of an aqueous chlorpyrifos solution (20 mg/L). The mixture was then stirred in a dark environment for 30 min to establish adsorption-desorption equilibrium [27]. For the photocatalytic degradation experiments, this solution was placed in the aforementioned photocatalytic reactor, with continuous aeration *via* a pump to maintain a uniform catalyst suspension throughout the reaction period. Samples (5 mL each) were withdrawn at fixed intervals of 10 min and centrifuged for 10 min to separate the nanocatalyst for reuse. The supernatant was subsequently analyzed using a UV-visible double-beam spectrophotometer at the maximum absorbance wavelength of chlorpyrifos (λ_{max} = 291 nm) to determine the pollutant concentration in solution [28,29].

The degradation efficiency of pollutants was calculated using the following equation:

$$\text{Degradation (\%)} = \frac{C_o - C_t}{C_o} \times 100 \quad (1)$$

where C_o (initial concentration) and C_t (concentration at a given time, t) denote the levels of organic pollutants before and after photo-irradiation, respectively.

RESULTS AND DISCUSSION

Phase structure analysis: The powder X-ray diffraction (XRD) analysis was conducted to examine the crystalline phase structure of SnO_2 nanoparticles. The XRD pattern of the synthesized SnO_2 sample, as illustrated in Fig. 1, exhibits well-defined diffraction peaks at specific 2θ angles, including 26.7º, 33.97º, 38º, 51.8º, 54.8º and 66.1º. These peaks correspond to the crystallographic planes (110), (101), (200), (211), (220) and (301), respectively [30]. The observed diffraction peaks matched well with the standard reference pattern from the Joint Committee on Powder Diffraction Standards (JCPDS No. 41-1445), confirming the presence of a cassiterite crystalline phase. The cassiterite phase is known to adopt a tetragonal rutile type crystal structure, characterized by a compact and thermodynamically stable arrangement of Sn and O atoms [30,31]. The sharp and intense nature of the peaks further suggests a high degree of crystallinity in the synthesized SnO_2 sample, indicating well-formed crystalline domains with minimal structural defects [32].

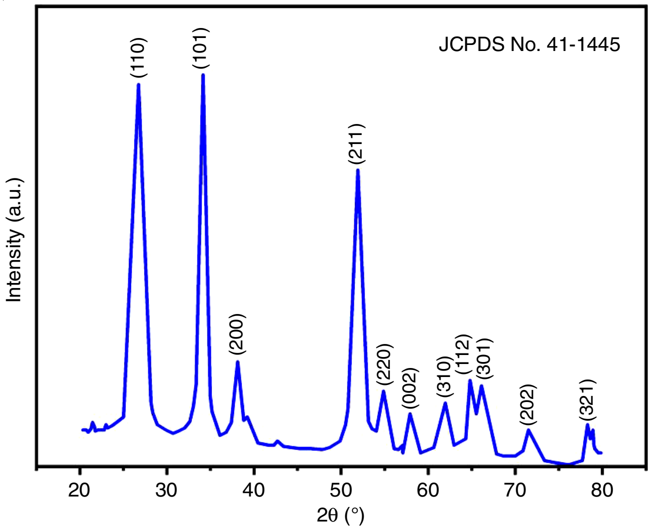

Fig. 1. XRD study of the SnO_2 nanoparticle

FTIR spectra: The FTIR spectrum of SnO_2 nanoparticles (Fig. 2) exhibits bands at approximately 554 cm^{-1} and 618 cm^{-1}, which correspond to Sn–O stretching vibrations associated with Sn–OH and Sn–O–Sn bonds, respectively [33,34]. Furthermore, the bands observed at around 1630 cm^{-1} and 3410 cm^{-1} are attributed to the bending vibrations of adsorbed water molecules on the SnO_2 surface and the stretching vibrations of –OH groups, respectively. These bands are primarily due to moisture absorption during sample preparation [35].

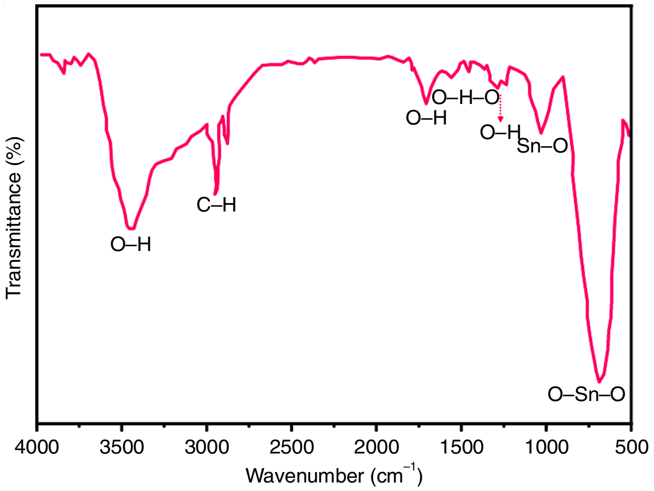

Fig. 2. FTIR spectra of the SnO_2 nanoparticle

Morphological studies: The morphology and structural characteristics of the SnO_2 nanostructures were thoroughly analyzed using scanning electron microscopy (SEM). Fig. 3 provides a detailed visualization of these intricate formations, revealing a diverse array of nanostructures. The SEM images depict the presence of low-lying spherical particles alongside elongated nanorods, which are systematically arranged in dense, bush-like formations [36]. Notably, the spherical exhibit hemispherical ends that extend outward, contributing to the overall complexity and high surface area of the SnO_2 structures. This unique morphology is expected to play a crucial role in enhancing the material's properties, particularly in applications requiring high surface-to-volume ratios, such as photocatalysis and sensor technologies [10,35].

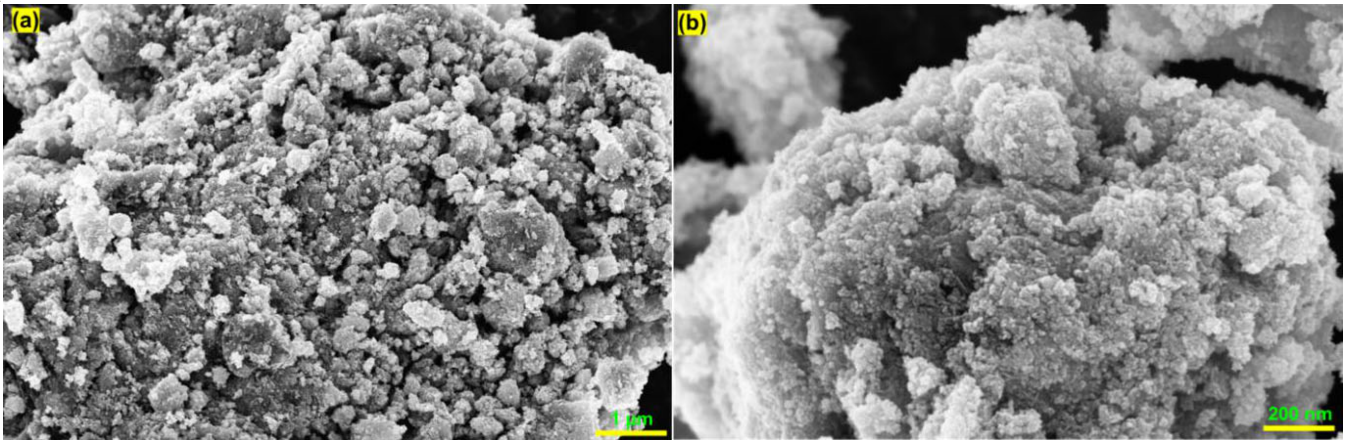

Fig. 3. SEM micrographs of the as prepared SnO_2 photocatalyst

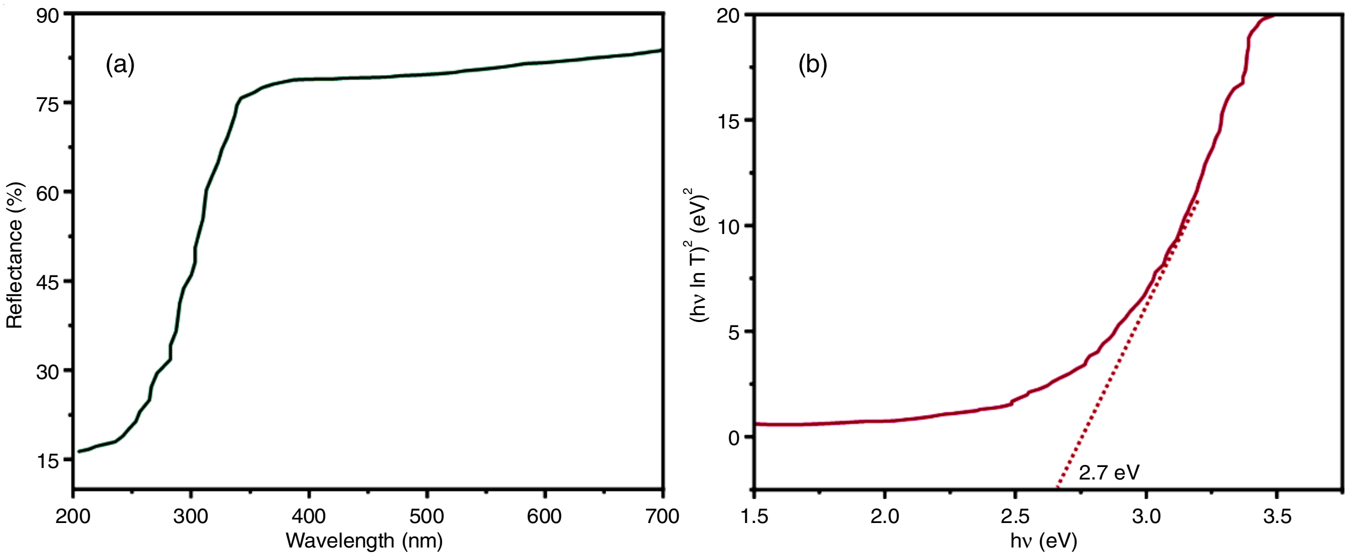

Fig. 4. (a) UV-vis DRS spectra and (b) the consistent bandgap values *via* Tauc plot of the synthesised nanoparticles

UV-DRS studies: The UV-Vis absorption spectrum of the synthesized SnO_2 nanoparticles is depicted in Fig. 4. The spectrum clearly shows that the absorption onset of the SnO_2 nanoparticles occurs at approximately 290 nm when the sample is calcined at 700 ºC [4]. This absorption edge (Fig. 4a) corresponds to the electronic transition from the valence band to the conduction band, indicating the optical properties of the material [37].

To further analyze the optical band gap energy (E_g) of the SnO_2 nanoparticles, a Tauc plot was constructed using the absorption spectra. The Tauc method involves plotting $(\alpha h\nu)^n$ *versus* photon energy (hν), where α is the absorption coefficient, hν is the photon energy and n depends on the nature of electronic transition (n = 2 for direct allowed transitions and n = ½ for indirect allowed transitions) [20]. By extrapolating the linear region of the plot to the energy axis, the estimated band gap energy of the SnO_2 nanoparticles was determined to be 2.7 eV shown in Fig. 4b. This band gap value is in good agreement with previously reported values for SnO_2, confirming its wide band gap semiconductor nature, which is suitable for various optoelectronic and photocatalytic applications [38].

The correlation between the absorption coefficient and the incident photon energy was established using eqn. 2:

$$F(R) = \frac{(1 \times R)^2}{2R} \quad (2)$$

where R stands for measured reflectance.

The bandgap energy (E_g) value is estimated using Tauc equation:

$$(\alpha h\nu)^2 = A(h\nu - E_g) \quad (3)$$

where hν represents the incident photon energy, K is a constant, E_g denotes the band gap energy and α(ν) is the absorption coefficient, which can be defined using Beer-Lambert's law.

Photoluminescence study: The photoluminescence (PL) spectrum provides valuable insights into the role of curcumin in improving the quantum efficiency of charge carrier separation, as illustrated in Fig. 5. The spectrum reveals two distinct emission peaks located at 350 nm and 750 nm, which correspond to the radiative recombination of photogenerated charge carriers. A key observation in this analysis is that a lower PL intensity signifies a reduced recombination rate of photogenerated electron-hole pairs, thereby enhancing the photocatalytic activity of the material [11,39].

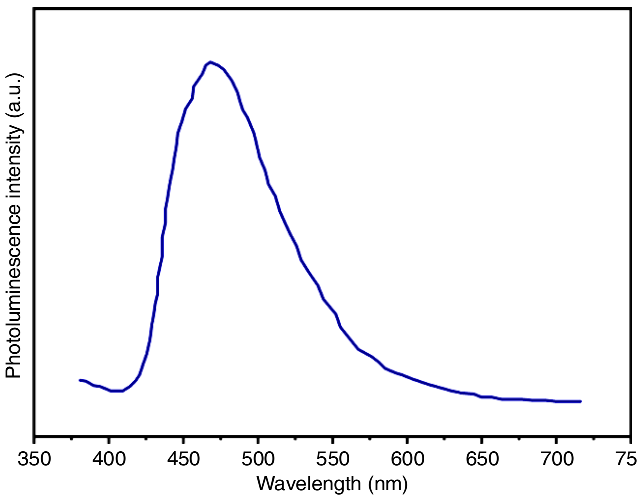

Fig. 5. Photoluminescence spectroscopy

Notably, when comparing the PL intensity of pristine SnO_2 with that of the curcumin-modified SnO_2 (curcumin/SnO_2), a significant reduction in emission intensity is observed. This decrease in PL intensity indicates that curcumin plays a crucial role in effectively suppressing charge carrier recombination [30]. By doing so, curcumin facilitates prolonged charge carrier lifetimes and enhances the generation of reactive radicals, which are essential for improved photocatalytic performance. Thus, the incorporation of curcumin into SnO_2 contributes to a more efficient charge separation process, ultimately leading to enhanced photocatalytic efficiency [18].

Photocatalytic degradation of aqueous chlorpyrifos: The photocatalytic efficiency of SnO_2 nanocatalyst was evaluated based on the photodegradation of an aqueous chlorpyrifos solution under UV-visible light irradiation. The reduction in the intensity of chlorpyrifos (λ_{max} = 291 nm) observed in the UV absorption spectrum confirmed the degradation of chlorpyrifos over time t (min) [22]. Fig. 6a illustrates the degradation process of chlorpyrifos using the SnO_2 nanocatalyst. Among the tested conditions, 78.8% of chlorpyrifos ($k = 0.0174$ min^{-1}) was degraded within 90 min under UV-visible light irradiation. The degradation rate constant of SnO_2 is depicted in Fig. 6b, while its degradation efficiency in percentage is presented in Fig. 6c. Moreover, the pseudo-first-order kinetics of chlorpyrifos photodegradation is shown in Fig. 6b.

Furthermore, the optimized addition of SnO_2 exhibited higher degradation efficiency, indicating enhanced visible light absorption and a significant reduction in the recombination of photo-excited electron-hole pairs. This ultimately promoted the generation of reactive oxidant species, facilitating the degradation of chlorpyrifos [40].

The equation, where C_t represents the chlorpyrifos concentration at different time intervals (t) and $C_t = 0$ denotes the initial concentration of chlorpyrifos, is given as follows:

$$\text{Degradation rate, } \eta\ (\%) = \frac{C_{t=0} - C_t}{C_t} \times 100 \qquad (4)$$

Moreover, the reaction kinetics were analyzed using a pseudo-first-order kinetic model, expressed as:

$$\ln\frac{C_o}{C_t} = kt \qquad (5)$$

where C_o (mg/L) and C_t (mg/L) correspond to the initial and residual CPF concentrations during the reaction, while k (mni^{-1}) and t (min) represent the apparent rate constant and reaction time, respectively.

Carriers trapping experiments and stability: As illustrated in Fig. 7b, different scavengers were employed in the photocatalytic process to neutralize reactive species. In this study, three primary reactive species ($^{\bullet}O^{2-}$, h^+ and $^{\bullet}OH$) were generated and contributed to the reaction [36]. Benzoquinone (BQ) was used to capture $^{\bullet}O^{2-}$, whereas potassium iodide (KI) and isopropanol (IPA) served as scavengers for h^+ and $^{\bullet}OH$, respectively, during chlorpyrifos degradation using the SnO_2 photocatalyst under visible light [41]. The chlorpyrifos degradation efficiency declined from 78.8% (without scavengers) to 76.8% (KI), 40.6% (IPA) and 55.2% (BQ). These findings indicate that the reactive species involved in pollutant degradation followed the order BQ > IPA > KI, highlighting that h^+ played a more significant role than $^{\bullet}OH$ and $^{\bullet}O^{2-}$ in CPF degradation.

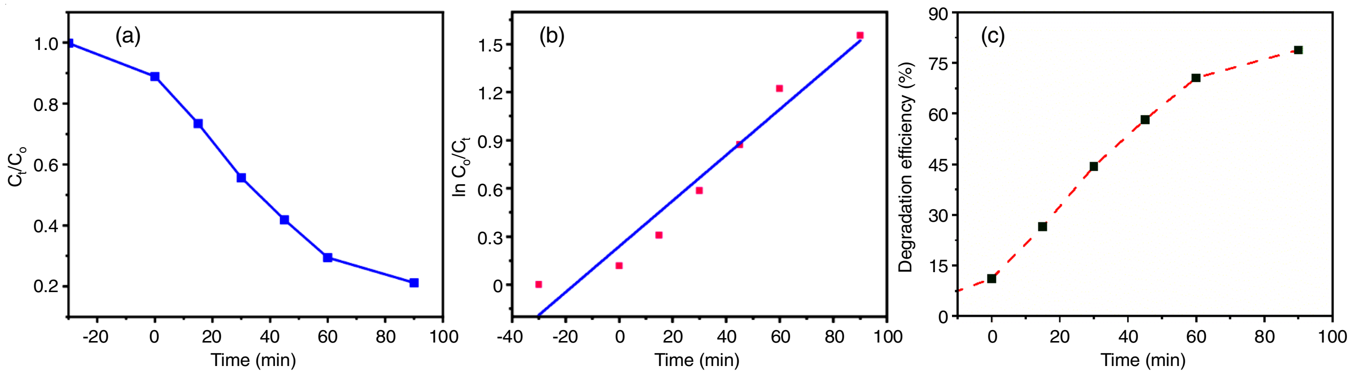

Fig. 6. a, b and c are the rate of CPF photodegradation, photodegradation effectiveness, and pseudo-first-order kinetic graphs for CPF using the obtained photocatalytic samples, along with the percentage of CPF pollutant degradation efficiency in the SnO_2 photocatalyst

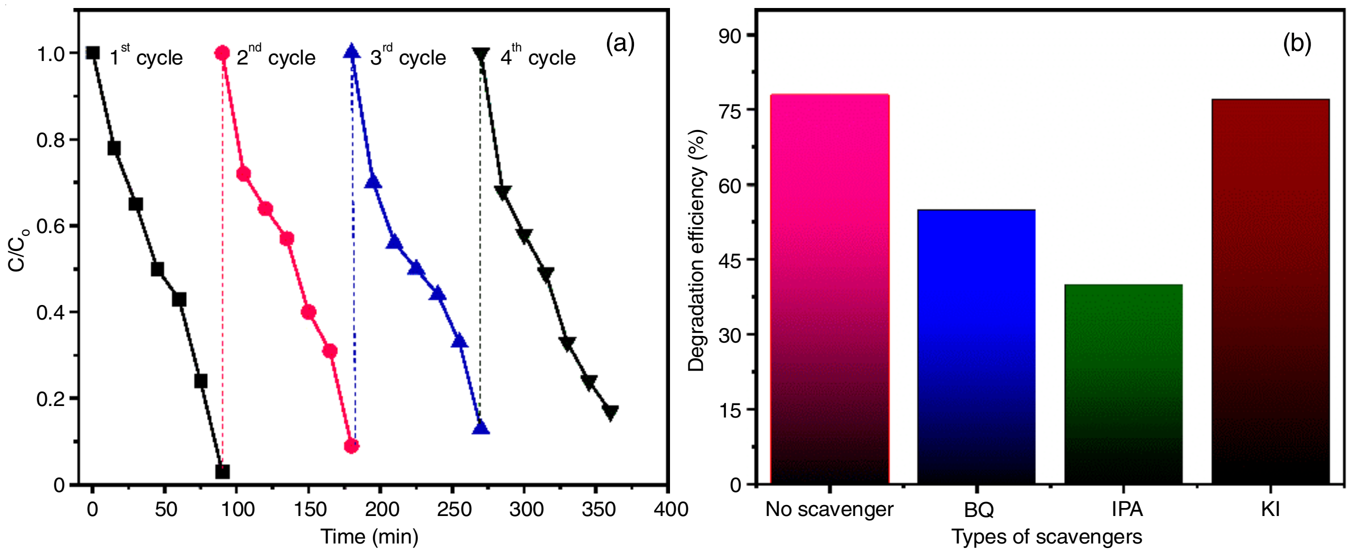

Fig. 7. (a) Recycling stability efficiency of the SnO_2 photocatalytic nanocomposite and (b) impact of reactive scavenging species on the photodegradation performance of CPF pollutants using the SnO_2 photocatalytic nanocomposite under visible-light irradiation

The stability of the photocatalyst was assessed by examining the recyclability of SnO_2 nanocatalyst through four consecutive cycling experiments for chlorpyrifos photodegradation. After each cycle, the samples were centrifuged, thoroughly washed with deionized water to remove any residual contaminants and subsequently dried in an oven at 60 ºC for reuse in the next cycle [42]. As shown in Fig. 7a, with a 90 min interval between cycles, approximately 78.8 % of chlorpyrifos was degraded in the first cycle. This efficiency exhibited a slight decline (~3.7%) in the second cycle (~75.1%), followed by further reductions in the third (~71.4%) and fourth (~67.7%) cycles [43].

Visible-light photocatalytic mechanism: Scheme-I illustrates the proposed mechanism underlying the enhanced photocatalytic degradation of chlorpyrifos over SnO_2 nanocatalyst. Under visible light irradiation, electron-hole pairs are generated as electrons are excited from the valence band (VB) to the conduction band (CB), leaving behind holes in the VB [32]. These photogenerated electrons (e^-) interact with oxygen (O_2), while the holes (h^+) react with hydroxyl ions (OH^-), forming reactive oxygen species such as superoxide radicals ($^{\bullet}O_2^-$) and hydroxyl radicals ($^{\bullet}OH$). These radicals play a crucial role in breaking down organic pollutants into harmless byproducts like H_2O and CO_2 [36]. Consequently, the high photocatalytic efficiency of the SnO_2 nanocatalyst is attributed to its effective charge separation and the efficient transfer of photoinduced charge carriers.

$$SnO_2 + h\nu \longrightarrow e^- + h^+ \qquad (6)$$

$$e^- + O_2 \longrightarrow {}^{\bullet}O_2^- \qquad (7)$$

$$2e^- + O_2 + 2H^+ \longrightarrow H_2O_2 \qquad (8)$$

$$h^+ + OH^- \longrightarrow {}^{\bullet}OH + H^+ \qquad (9)$$

$${}^{\bullet}OH + h^+ + CPF \longrightarrow \text{Degradation pollutants} \qquad (10)$$

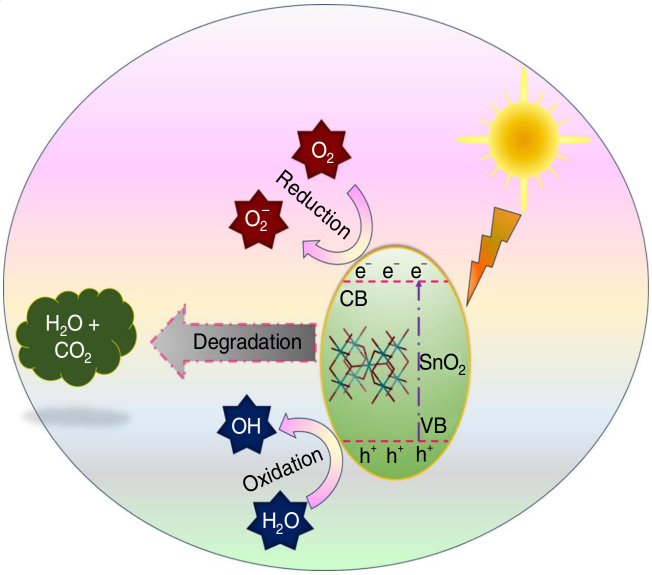

Scheme-I: The possible reaction mechanism of CPF SnO_2 nanocomposite system

Conclusion

The study successfully demonstrated the effectiveness of SnO_2 as a photocatalyst for wastewater decontamination under visible light exposure. The synthesized SnO_2 nanoparticles exhibited significantly high photocatalytic activity, achieving an impressive 78.8% degradation of chlorpyrifos within 90 min. The apparent rate constant (K_{app}) for chlorpyrifos degradation using the SnO_2 nanoparticles was determined to be 0.0174 min^{-1}, indicating its efficient degradation kinetics. Furthermore, the nanoparticles exhibited remarkable durability and stability, as evidenced by its consistent performance over four consecutive recycling tests. The catalyst retained its photocatalytic efficiency and was easily recoverable, highlighting its potential for long-term practical applications. Overall, this research presents a successfully fabricated SnO_2-based nanocatalyst with high photocatalytic efficiency, stability and recyclability.

ACKNOWLEDGEMENTS

This work is supported by the Natural Products & Nanobiotechnology Research Lab, Saveetha Medical College and Hospital, Saveetha Institute of Medical and Technical Sciences, Chennai, India.

CONFLICT OF INTEREST

The authors declare that there is no conflict of interests regarding the publication of this article.

REFERENCES

1. M.V. Arularasu, M. Harb and R. Sundaram, *Carbohydr. Polym.*, **249**, 116868 (2020); https://doi.org/10.1016/j.carbpol.2020.116868
2. S. Sankeshi, P. Bajaj, V.P. Sivasankaran, M.V. Sunkara and P. Basak, *ACS Appl. Mater. Interfaces*, **17**, 3757 (2025); https://doi.org/10.1021/acsami.4c17092
3. M. Kaur, D. Prasher and R. Sharma, *J. Water Environ. Nanotechnol.*, **7**, 194 (2022); https://doi.org/10.22090/jwent.2022.02.007
4. G. Ramanathan and K.R. Murali, *J. Appl. Electrochem.*, **52**, 849 (2022); https://doi.org/10.1007/s10800-022-01676-z
5. G.B. Nam, J.-E. Ryu, T.H. Eom, S.J. Kim, J.M. Suh, S. Lee, S. Choi, C.W. Moon, S.J. Park, S.M. Lee, B. Kim, S.H. Park, J.W. Yang, S. Min, S. Park, S.H. Cho, H.J. Kim, S.E. Jun, T.H. Lee, Y.J. Kim, J.Y. Kim, Y.J. Hong, J.-I. Shim, H.-G. Byun, Y. Park, I. Park, S.-W. Ryu and H.W. Jang, *Nano-Micro Lett.*, **16**, 261 (2024); https://doi.org/10.1007/s40820-024-01486-2
6. N.Y. Elamin, T. Indumathi and E.R. Kumar, *Ceram. Int.*. **49**, 2388 (2023); https://doi.org/10.1016/j.ceramint.2022.09.211
7. C. Liu, M. Han, C.-L. Chen, J. Yin, L. Zhang and J. Sun, *Nano Lett.*, **23**, 3507 (2023); https://doi.org/10.1021/acs.nanolett.3c00656
8. M. Manimaran, A. Muthuvel and N.M. Said, *Nanotechnol. Environ. Eng.*, **8**, 413 (2023); https://doi.org/10.1007/s41204-022-00297-3
9. M. Arif, M.Z.U. Shah, S.A. Ahmad, M.S. Shah, Z. Ali, A. Ullah, M. Idrees, J. Zeb, P. Song, T. Huang and J. Yi, *Opt. Mater.*, **134**, 113135 (2022); https://doi.org/10.1016/j.optmat.2022.113135
10. G.H. Patel, S.H. Chaki, R.M. Kannaujiya, Z.R. Parekh, A.B. Hirpara, A.J. Khimani and M.P. Deshpande, *Physica B*, **613**, 412987 (2021); https://doi.org/10.1016/j.physb.2021.412987
11. J. He, H. Meng, X. Wang, Y. Xu and L. Feng, *Sens. Actuators B Chem.*, **418**, 136335 (2024); https://doi.org/10.1016/j.snb.2024.136335

12. E. Skripkin, A.A. Podurets, D. Kolokolov, A. Burmistrova, N. Bobrysheva, M. Osmolowsky, M.A. Voznesenskiy and O. Osmolovskaya, *ACS Omega*, **7**, 6093 (2021); https://doi.org/10.1021/acsomega.1c00043
13. M.C. Uribe-López, M.C. Hidalgo-López, R. López-González, D.M. Frías-Márquez, G. Núñez-Nogueira, D. Hernández-Castillo and M.A. Alvarez-Lemus, *J. Photochem. Photobiol. A: Chem.*, **404**, 112866 (2021); https://doi.org/10.1016/j.jphotochem.2020.112866
14. M.G. Kim, J.M. Kang, J.E. Lee, K.S. Kim, K.H. Kim, M. Cho and S.G. Lee, *ACS Omega*, **6**, 10668 (2021); https://doi.org/10.1021/acsomega.1c00043
15. S.K. Rahi, R.A. Al-Wardy and H.A.A.T. Al Ogaili, *Baghdad Sci. J.*, **22**, 1252 (2025); https://doi.org/10.21123/bsj.2024.8208
16. M.A. Shilpa Amulya, H.P. Nagaswarupa, M.R. Anil Kumar, C.R. Ravikumar, K.B. Kusuma and S.C. Prashantha, *J. Phys. Chem. Solids*, **148**, 109756 (2021); https://doi.org/10.1016/j.jpcs.2020.109756
17. J. Mou, Y. Ren, J. Wang, C. Wang, Y. Zou, K. Lou, Z. Zheng and D. Zhang, *Microfluid Nanofluid*, **26**, 25 (2022); https://doi.org/10.1007/s10404-022-02534-2
18. D. Letsholathebe, F. Thema, K. Mphale, H.EA. Mohamed, K.J. Holonga, R. Ketlhwaafetse and S. Chimidza, *Mater. Today: Proc.*, **36**, 499 (2021); https://doi.org/10.1016/j.matpr.2020.05.205
19. S.K. Jain, N.A. Pandit, M. Fazil, S.A. Ali, J. Ahmed, S.M. Alshehri, Y. Mao and T. Ahmad, *Nanotechnology*, **33**, 355706 (2022); https://doi.org/10.1088/1361-6528/ac705a
20. A. Al Baroot, K.A. Elsayed, S.A. Haladu, S.M. Magami, M. Alheshibri, F. Ercan, E. Çevik, S. Akhtar, A.A.Manda, T.S. Kayed, N.A. Altamimi, A.A. Alsanea and A.L. Al-Otaibi, *Opt. Laser Technol.*, **157**, 108734 (2023); https://doi.org/10.1016/j.optlastec.2022.108734
21. D. Chen and L. Gao, *Chem. Phys. Lett.*, **398**, 201 (2004); https://doi.org/10.1016/j.cplett.2004.09.055
22. R. Mahanta, P. Chetri and D. Bora, *Mater. Today: Proc.*, (2023); https://doi.org/10.1016/j.matpr.2023.04.348
23. B. Padmaja, S. Dhanapandian, K. Ashokkumar and N. Krishnakumar, *Inorg. Chem. Commun*., **155**, 110948 (2023); https://doi.org/10.1016/j.inoche.2023.110948
24. A.H. Pinto, A.E. Nogueira, C.J. Dalmaschio, I.N. Frigini, J.C. de Almeida, M.M. Ferrer, O.M. Berengue, R.A. Gonçalves and V.R. de Mendonça, *Solids*, **3**, 327 (2022); https://doi.org/10.3390/solids3020024
25. N.M. Al-Enazi, S. Alwakeel and E. Alhomaidi, *J. Appl. Microbiol.*, **133**, 3265 (2022); https://doi.org/10.1111/jam.15607
26. S. Sagadevan, J.A. Lett, S.F. Alshahateet, I. Fatimah, G.K. Weldegebrieal, M.-V. Le, E. Leonard, S. Paiman and T. Soga, *Inorg. Chem. Commun.* **141**, 109547 (2022); https://doi.org/10.1016/j.inoche.2022.109547
27. M.S. Khan, J.A. Shah, M. Arshad, S.A. Halim, A. Khan, A.J. Shaikh, N. Riaz, A.J. Khan, M. Arfan, M. Shahid, A. Pervez, A. Al-Harrasi and M. Bilal, *Molecules*, **25**, 4468 (2020); https://doi.org/10.3390/molecules25194468
28. C. Sun, J. Yang, Y. Zhu, M. Xu, Y. Cui, L. Liu, W. Ren, H. Zhao and B. Liang, *J. Alloys Comp.*, **871**, 159561 (2021); https://doi.org/10.1016/j.jallcom.2021.159561
29. B. Padmaja, S. Dhanapandian, S. Suthakaran, K. Ashokkumar and N. Krishnakumar, *Inorg. Chem. Commun.*, **149**, 110363 (2023); https://doi.org/10.1016/j.inoche.2022.110363
30. S.R. Kiran Kumar, S. Harisha, P. Jalaja, B.K. Jayanna, K.Y. Kumar and M.S. Anantha, *Sensors Int*., **5**, 100278 (2024); https://doi.org/10.1016/j.sintl.2023.100278
31. P. S. Vindhya & V. T. Kavitha, *J. Inorg. Organomet. Polym.*, **33**, 2873 (2023); https://doi.org/10.1007/s10904-023-02733-6
32. A.A. Podurets, E.V. Beletskii, E.V. Ubyivovk, N.P. Bobrysheva, M.G. Osmolowsky, M.A. Voznesenskiy and O.M. Osmolovskaya, *Mater. Chem. Phys.*, **290**, 126589 (2022); https://doi.org/10.1016/j.matchemphys.2022.126589
33. M. Anu and S.S. Pillai, *Solid State Commun.*, **341**, 114577 (2022); https://doi.org/10.1016/j.ssc.2021.114577
34. N. Rani, K. Khurana and N. Jaggi, *Surf. Interfaces*, **27**, 101492 (2021); https://doi.org/10.1016/j.surfin.2021.101492
35. S.S. Batros, S., M. Ali and A.J. Addie, *J. Appl. Sci. Nanotechnol.*, **3**, 20 (2023); https://doi.org/10.53293/jasn.2023.7107.1246
36. T. Preethi, K. Senthil, M.P. Pachamuthu, R. Balakrishnaraja, N. Geetha, B. Sundaravel and S. Bellucci, *Adsorpt. Sci. Technol.*, **2022**, 9334079 (2022); https://doi.org/10.1155/2022/9334079
37. K. Balakrishnan and N. Murugesan, *Int. J. Nano Dimens*., **12**, 76 (2021); https://doi.org/10.22034/ijnd.2021.677125
38. U. Altaf, M.Z. Ansari and S. Rubab, *Mater. Chem. Phys.*, **297**, 127304 (2023); https://doi.org/10.1016/j.matchemphys.2023.127304
39. P. Jithin, K. Sudheendran, K. Sankaran and J. Kurian, *Opt. Mater.*, **120**, 111367 (2021); https://doi.org/10.1016/j.optmat.2021.111367
40. S.A.A. Nami, M. Arshad, M.S. Khan, M. Alam, D.-U. Lee, S. Park and N. Sarikavakli, *Polym. Adv. Technol.*, **26**, 1627 (2015); https://doi.org/10.1002/pat.3591
41. I.N. Reddy, K. Ashok, D.R. Cuddapah, A. Bhargav, M. Dhanasekar, J. Shim and C. Bai, *Inorg. Chem. Commun.*, **167**, 112729 (2024); https://doi.org/10.1016/j.inoche.2024.112729
42. W.A.A. Mohamed, S.B. Moussa, H.H.A. El-Gawad, H.A. Mousa, H.T. Handal, H.R. Galal, I.A. Ibrahem, M.M. Fawzy, M.A.M. Ahmed, A.A. Labib and M.S.A. Abdel-Mottaleb, *J. Clust. Sci.*, **36**, 58 (2025); https://doi.org/10.1007/s10876-025-02772-8
43. Y. Wu, H. Wang, M. Cao, Y. Zhang, F. Cao, X. Zheng, J. Hu, J. Dong and Z. Xiao, *J. Nanosci. Nanotechnol.*, **15**, 6495 (2015); https://doi.org/10.1166/jnn.2015.10781